NASA Contractor Report 198197

Analysis of Elliptically Polarized Cavity Backed Antennas Using a Combined FEM/MoM/GTD Technique

C. J. Reddy
Hampton University, Hampton, Virginia

M. D. Deshpande
ViGYAN,Inc., Hampton, Virginia

D. T. Fralick
Lockheed Engineering & Sciences Company, Hampton, Virginia

Contract NAS1-19935

August 1995

National Aeronautics and
Space Administration
Langley Research Center
Hampton, Virginia 23681-0001

CONTENTS

ABSTRACT

Radiation pattern prediction analysis of elliptically polarized cavity backed aperture antennas in a finite ground plane is carried out using a combined Finite Element Method (FEM) / Method of Moments (MoM) / Geometrical Theory of Diffraction (GTD) technique. The magnetic current on the cavity-backed aperture in an infinite ground plane is calculated using the combined FEM / MoM analysis. GTD, including the slope diffraction contribution, is used to calculate the diffracted fields due to both soft and hard polarizations at the edges of the finite ground plane. Numerical results for the radiation patterns of a cavity backed circular spiral microstrip patch antenna excited by a coaxial probe in a finite rectangular ground plane are computed and compared with experimental results.

LIST OF SYMBOLS

∇	Del operator
ε_r	Relative permittivity
μ_r	Relative permeability
μ_o	Permeabilty of free space
η	Intrinsic impedance of free space
ρ_{cA}, ρ_{cB}	Defined in equation (15)
ξ_1, ξ_2	As defined in equations (16) and (17)
ω	Angular frequency
D_s	Soft diffraction coefficient
D_h	Hard diffraction coefficient
$\vec{E}$	Electric field
E_θ	Electric far field, θ component
E_ϕ	Electric far field, ϕ component
$\vec{H}_{ap}$	Magnetic field at the aperture
$\vec{H}_{inp}$	Magnetic field at the input plane
$H_{\theta ff}$	Magnetic far field, θ component
$H_{\phi ff}$	Magnetic far field, ϕ component
$H^d_{\theta A}$	Diffracted magnetic field at point A, θ component
$H^d_{\phi A}$	Diffracted magnetic field at point A, ϕ component
$H^d_{\theta B}$	Diffracted magnetic field at point B, θ component
$H^d_{\phi B}$	Diffracted magnetic field at point B, ϕ component
$H^d_{\theta C}$	Diffracted magnetic field at point C, θ component

$H^{d}_{\phi C}$	Diffracted magnetic field at point C, ϕ component
$H^{d}_{\theta D}$	Diffracted magnetic field at point D, θ component
$H^{d}_{\phi D}$	Diffracted magnetic field at point D, ϕ component
$H^{t}{}_{\theta ff}$	Total magnetic far field after adding the diffracted field, θ component
$H^{t}{}_{\phi ff}$	Total magnetic far field after adding the diffracted field, ϕ component
j	$\sqrt{-1}$
k_o	Free space wavenumber
k_x	Fourier transform variable with respect to x
k_y	Fourier transform variable with respect to y
$\vec{M}$	Magnetic current in the aperture
M_x	x-component of magnetic current
M_y	y-component of magnetic current
$\tilde{M}_x$	Fourier transform of M_x (equation (7))
$\tilde{M}_y$	Fourier transform of M_y (equation (8))
$\hat{n}$	unit normal
r, θ, ϕ	Spherical coordinates
S_{11}	Return loss(dB)
S_{ap}	Integration over the aperture surface
S_{inp}	Integration over the input plane
$\vec{T}$	Testing function
V	Integration over the volume
W_1, W_2	Dimensions of the finite ground plane
X,Y,Z	Cartesian coordinates

1. INTRODUCTION

Cavity backed antennas are important in aerospace and automobile applications due to their conformal nature. Previously a combined FEM/MoM/GTD technique has been applied to linearly polarized cavity backed antennas in a finite ground plane[1]. In this method, the far field due to the magnetic current in the aperture is considered to be incident on the edge of the finite ground plane to produce the diffracted field. In GTD, when the electric field is normal to the edge of the ground plane, it is referred to as *hard polarization* and when it is tangential to the edge of the ground plane it is referred to as *soft polarization*. For soft polarization, the electric field incident at the diffraction point on the ground plane is zero. In such cases, GTD may be used with slope diffraction. Slope diffraction is based not on the magnitude of the incident field at the point of diffraction, but rather on the slope magnitude of the incident field at the point of diffraction.

The application of slope diffraction to cavity backed antennas is given in detail in reference[2]. In the present report, a combined FEM/MoM method is used to analyze the elliptically polarized cavity backed antennas in a finite ground plane. GTD, with slope diffraction coefficients is used to augment the radiation patterns of these antennas on a finite ground plane. A particular case of a cavity-backed Archimedean spiral microstrip antenna fed by the center conductor of a coaxial line is considered. For this elliptically polarized antenna, GTD along with slope diffraction is used to account for the radiation patterns of both E_θ and E_ϕ polarizations. The radiation patterns of the spiral antenna are calculated and compared with experimental results measured at NASA Langley Research Center’s Low Frequency Antenna Measurement Facility. Good agreement between the calculated and measured data is obtained.

2. THEORY

The geometry of the problem to be analyzed is shown in figure 1. For a linear, isotropic and source free region the electric field satisfies the vector wave equation

$$\nabla\times\left(\frac{1}{\mu_r}\nabla\times\vec{E}\right)-k_o^2\varepsilon_r\vec{E} = 0 \tag{1}$$

where μ_r and ε_r are the relative permeability and permittivity respectively of the medium in the cavity. The time variation $\exp(j\omega t)$ is assumed and suppressed throughout this paper.

To facilitate the solution of the partial differential equation in (1) for the cavity via FEM, equation (1) is multiplied by a vector testing function $\vec{T}$ and the result is integrated over the volume of the cavity. By applying suitable vector identities, equation (1) can be written in its weak form[8] as

$$\iiint\limits_V \frac{1}{\mu_r}\left(\nabla\times\vec{T}\right)\bullet\left(\nabla\times\vec{E}\right)dv-k_o^2\varepsilon_r\iiint\limits_V\vec{T}\bullet\vec{E}dv = \iiint\limits_V\nabla\bullet\left(\vec{T}\times\frac{1}{\mu_r}\nabla\times\vec{E}\right)dv \tag{2}$$

Applying the divergence theorem to the integral on the right hand side of equation (2) and using Maxwell's equation $\nabla\times\vec{E} = -j\omega\mu_o\mu_r\vec{H}$, where μ_o, is the permeability of free space and ω is the angular frequency, equation (2) can be rewritten as

$$\iiint\limits_V \frac{1}{\mu_r}\left(\nabla\times\vec{T}\right)\bullet\left(\nabla\times\vec{E}\right)dv-k_o^2\varepsilon_r\iiint\limits_V\vec{T}\bullet\vec{E}dv = j\omega\mu_o\iint\limits_S\left(\vec{T}\times\hat{n}\right)\bullet\vec{H}ds \tag{3}$$

where $\hat{n}$ is the unit outward normal to the surface and $\vec{H}$ is the magnetic field on the surface of the cavity. As the tangential electric field is zero on the perfect electric conducting (PEC) walls of the cavity, the surface integral in equation(3) is nonzero only over the aperture opening in the infinite ground plane and the input aperture.

$$\iiint_V \frac{1}{\mu_r}\left(\nabla\times\vec{T}\right)\bullet\left(\nabla\times\vec{E}\right)dv - k_o^2\varepsilon_r\iiint_V \vec{T}\bullet\vec{E}dv - j\omega\mu_o\int\int_{S_{ap}}\left(\vec{T}\times\hat{n}\right)\bullet\vec{H}_{ap}ds$$

$$= \quad j\omega\mu_o\int\int_{S_{inp}}\left(\vec{T}\times\hat{n}\right)\bullet\vec{H}_{inp}ds \tag{4}$$

where S_{ap} is the aperture surface and S_{inp} is the input surface (see fig. 1). $\vec{H}_{ap}$ is the magnetic field at the aperture and $\vec{H}_{inp}$ is the magnetic field at the input surface.

At this point, the problem can be divided into three parts, the first part involving the discretization and evaluation of volume integrals on the left hand side of equation (4) and the second part involving the discretization and evaluation of the surface integral over S_{ap}. The third part involves the surface integral over the input aperture. The volume integral is evaluated by discretizing the volume of the cavity with tetrahedral elements and evaluating the integral over the volume of each tetrahedral element. These element volume integral contributions are added together over all tetrahedral elements to form a sparse matrix. The second integral is evaluated over the surface of the aperture. The discretization of the volume of the cavity into tetrahedral elements automatically discretizes the aperture surface into triangular elements. Assuming the current basis functions similar to that described in [3], an integral equation is formed, which contributes to the dense part of the system matrix. Image theory is used to account for the presence of the infinite ground plane. The third integral is evaluated over the input coaxial aperture surface and forms the excitation column matrix. Solving for the system matrix formed by these three integrals, the electric fields in the cavity are obtained and hence the magnetic current $\vec{M}$ in the aperture S_{ap}.

Using the magnetic current $\vec{M}(x, y)$ over the aperture, the magnetic far field is given by the following equations:

$$H_{\theta ff}(r, \theta, \phi) = -\frac{jk_o}{\eta}\frac{\exp(-jk_or)}{2\pi r}\cos\theta\left[\tilde{M}_x(k_x, k_y)\cos\phi + \tilde{M}_y(k_x, k_y)\sin\phi\right] \tag{5}$$

$$H_{\phi ff}(r, \theta, \phi) = -\frac{jk_o}{\eta}\frac{\exp(-jk_or)}{2\pi r}\left[\tilde{M}_y(k_x, k_y)\cos\phi - \tilde{M}_x(k_x, k_y)\sin\phi\right] \tag{6}$$

where

$$\tilde{M}_x(k_x, k_y) = \iint_{S_a} M_x(x, y)\exp\{j(k_x x + k_y y)\}\,dxdy \tag{7}$$

and

$$\tilde{M}_y(k_x, k_y) = \iint_{S_a} M_y(x, y)\exp\{j(k_x x + k_y y)\}\,dxdy \tag{8}$$

$$k_x = k_o\cos\phi\sin\theta \tag{9}$$

$$k_y = k_o\sin\phi\sin\theta \tag{10}$$

Using equations (5) and (6), radiation patterns in the forward direction of a cavity backed antenna in infinite ground plane are computed. The effect of the finite ground plane is incorporated by employing the edge diffraction coefficients along with the slope diffraction coefficients. The radiation fields are supplemented by the additional field contributions arising from the diffraction by the edges of the finite ground plane. The diffracted field supplements the field in the forward direction, whereas it accounts totally for the field in the shadow region (behind the finite ground plane) where the infinite ground plane solution gives a zero field.

The geometry of the finite ground plane is illustrated in figure 1. The midpoints on the two edges of length W_2 are given by A and B, respectively, whereas the midpoints on the two edges of length W_1 are given by C and D, respectively. The total diffracted field at A and B are given by [2,6]

$$H^{d}_{\theta A} \sim \frac{1}{2}\left\{ H_{\theta ff}\left(d, \frac{\pi}{2}, 0\right) D_s\,(\rho_{cA}, \xi_1, \psi', \beta'_o, n) + \frac{1}{jk_o}\left(\left.\frac{\partial H_{\theta ff}}{\partial \theta}\right|_{d,\, \frac{\pi}{2},\, 0}\right)\left(\left.\frac{\partial D_s}{\partial \psi'}\right|_{\rho_{cA},\, \xi_1,\, \psi',\, \beta'_o,\, n}\right)\right\}$$
$$\left[\frac{\rho_{cA}}{r}\right]^{1/2} exp\,(-jk_o r)\; exp\,(jk_o d \sin\theta) \tag{11}$$

$$H^{d}_{\theta B} \sim \frac{1}{2}\left\{ H_{\theta ff}\left(d, \frac{\pi}{2}, \pi\right) D_s\,(\rho_{cB}, \xi_2, \psi', \beta'_o, n) + \frac{1}{jk_o}\left(\left.\frac{\partial H_{\theta ff}}{\partial \theta}\right|_{d,\, \frac{\pi}{2},\, \pi}\right)\left(\left.\frac{\partial D_s}{\partial \psi'}\right|_{\rho_{cB},\, \xi_2,\, \psi',\, \beta'_o,\, n}\right)\right\}$$
$$\left[\frac{\rho_{cA}}{r}\right]^{1/2} exp\,(-jk_o r)\; exp\,(-jk_o d \sin\theta) \tag{12}$$

for ϕ polarization, and

$$H^{d}_{\phi A} \sim \frac{1}{2}\left\{ H_{\phi ff}\left(d, \frac{\pi}{2}, 0\right) D_h\,(\rho_{cA}, \xi_1, \psi', \beta'_o, n) + \frac{1}{jk_o}\left(\left.\frac{\partial H_{\phi ff}}{\partial \theta}\right|_{d,\, \frac{\pi}{2},\, 0}\right)\left(\left.\frac{\partial D_h}{\partial \psi'}\right|_{\rho_{cA},\, \xi_1,\, \psi',\, \beta'_o,\, n}\right)\right\}$$
$$\left[\frac{\rho_{cA}}{r}\right]^{1/2} exp\,(-jk_o r)\; exp\,(jk_o d \sin\theta) \tag{13}$$

$$H_{\phi B}^{d} \sim \frac{1}{2}\left\{H_{\phi ff}\left(d, \frac{\pi}{2}, \pi\right)D_h\,(\rho_{cB}, \xi_2, \psi', \beta'_o, n) + \frac{1}{jk_o}\left(\left.\frac{\partial H_{\phi ff}}{\partial\theta}\right|_{d, \frac{\pi}{2}, \pi}\right)\left(\left.\frac{\partial D_h}{\partial\psi'}\right|_{\rho_{cB}, \xi_2, \psi', \beta'_o, n}\right)\right\}$$

$$\left[\frac{\rho_{cA}}{r}\right]^{1/2} exp\,(-jk_o r)\; exp\,(-jk_o d\sin\theta) \qquad (14)$$

for θ polarization. In the above equations,

$$\rho_{cA} = \rho_{cB} = d = \frac{W_1}{2} \qquad (15)$$

and

$$\xi_1 = \frac{\pi}{2} + \theta \qquad 0 \le \theta \le \pi \qquad (16)$$

$$\xi_2 = \begin{cases} \dfrac{\pi}{2} - \theta & 0 \le \theta \le \dfrac{\pi}{2} \\ \dfrac{5\pi}{2} - \theta & \dfrac{\pi}{2} \le \theta \le \pi \end{cases} \qquad (17)$$

ψ' =Angle of incidence from the aperture(source) toward the point of diffraction(A or B) $=0^o$

$\beta'_o = \frac{\pi}{2}$ for normal incidence[6, pp.811]

n=wedge factor[6, figure 13-30]

Similarly, the diffracted fields at C and D are also calculated by replacing $\rho_{cC} = \rho_{cD} = d = \frac{W_2}{2}$. The detailed expressions for diffraction coefficients $D_{s/h}$ are given by [6, eq.13-89]. The slope diffraction coefficients are given in [2]. The total diffracted field is given by

$$H_\theta^d = \begin{cases} H_{\theta A}^d + H_{\theta B}^d & \phi = 0^o \ \ plane \\ H_{\theta C}^d + H_{\theta D}^d & \phi = 90^o \ \ plane \end{cases} \tag{18}$$

and

$$H_\phi^d = \begin{cases} H_{\phi A}^d + H_{\phi B}^d & \phi = 0^o \ \ plane \\ H_{\phi C}^d + H_{\phi D}^d & \phi = 90^o \ \ plane \end{cases} \tag{19}$$

The diffracted fields for $\phi = 180^o$ and $\phi = 270^o$ planes can also be calculated in a similar manner. The total radiated far field is given by adding the diffracted magnetic field and magnetic far field given in equations (5) and (6); *i.e.*,

$$H^t{}_{\theta ff} = H_{\theta ff} + H_\theta^d \tag{20}$$

$$H^t{}_{\phi ff} = H_{\phi ff} + H_\phi^d \tag{21}$$

The radiated electric far field is given by

$$E_\theta = \eta H^t{}_{\phi ff} \tag{22}$$

$$E_\phi = \eta H^t{}_{\theta ff} \tag{23}$$

Using the magnetic current in the aperture in equations (5) and (6) and evaluating equations (20),(21), (22) and (23), the radiation patterns of the cavity-backed aperture antennas with a finite rectangular ground plane are computed.

3. NUMERICAL AND EXPERIMENTAL RESULTS

To verify the validity of the analysis presented, a cavity-backed spiral microstrip antenna in a finite rectangular ground plane is considered. The spiral microstrip antenna is designed to produce elliptical polarization. The geometry of the spiral antenna is shown in figure 2. A two and a half turn, two arm circular Archimedean spiral is designed to be fed at the center by the center conductor of the coaxial probe. The substrate is 1/16” thick with a relative dielectric constant of 2.33. The width of the spiral is designed to be 2/23”. The microstrip spiral antenna is placed in a 2” diameter cavity of 1/16” depth with a rectangular ground plane of 24” length and 12” width.

3.1 Experimental Procedure:

The spiral antenna was fed at its center with the center conductor of RG-141 coaxial semi-rigid cable. The copper shield was conductively bonded to the copper clad back side of the antenna. This back side provided a conductive path to the ground plane when placed in the machined cavity in the ground plane. The antenna/ ground plane assembly was then placed on the roll-over-azimuth-over-elevation positioning system in the NASA Langley Research Center Low Frequency Antenna Measurement Facility.

Electrical boresight was accomplished by sighting the characteristic null, normal to the plane of the antenna, of a spiral fed in the manner described. Calibration of the system was not performed as the data were normalized.

Principal plane measurements were accomplished for both polarizations, horizontal(E_{θ}) and vertical(E_{ϕ}), and for two orthogonal positions of the antenna, $\phi = 0^o, 180^o$ and $\phi = 90^o, 270^o$, shown in figure 2.

3.2 Numerical Modelling:

The cavity volume with the spiral antenna is modelled using a commercial package COSMOS/M[8] and meshed with 8,740 tetrahedral elements which resulted in 1820 triangular elements in the aperture surface. The radiation patterns for both horizontal (E_{θ}) polarization and vertical (E_{ϕ}) polarization are computed using equations (20) and (21) respectively. Figures 3 (a) and (b) are plots of normalized radiation patterns for horizontal polarization at $\phi = 0^o, 180^o$ and $\phi = 90^o, 270^o$ respectively at 4 GHz. It can be seen that the measured data and computed results agree very well. Figures 4 (a) and (b) are plots of normalized radiation patterns for vertical polarization at $\phi = 0^o, 180^o$ and $\phi = 90^o, 270^o$ respectively at 4 GHz. Good agreement between the computed and experimental results is found in the forward direction of the antenna. There is considerable disagreement in the backward direction. Possible causes for this disagreement are discussed in the following subsection. Similarly, computed results for normalized radiation patterns for both horizontal and vertical polarizations are plotted along with the experimental data in figures 5 and 6, respectively, at 5 GHz. The disagreement between the computed and measured results in figure 6 are discussed in the following subsections.

3.3 Experimental limitations :

Two primary contributions should be mentioned as possible sources of measurement error. The first is the poor return loss, S_{11}, of the spiral antenna used in the measurement. The antenna, fed as previously described with no balun or matching network, was matched poorly to the 50Ω measurement system. A *Wheeler can test*[9] was performed and indicated that most of the return loss that was measurable could be attributed to other than radiation resistance. Therefore, only small signal levels were coupled to the coaxial line feeding the antenna and caused a degradation of overall system dynamic range of the measurement set-up. The second inaccuracy was due to the placement of the remote mixer and relatively low signal levels mentioned above. Standard practice is to place the mixer as close as possible to the antenna under test. The mixer for these measurements was placed behind the ground plane, so that losses at the desired test frequency could be minimized. As a consequence, the mixer and the cable were directly illuminated for angles of $\theta \geq 90^o$. Although the cable and mixer are both shielded, neither are perfect. It is felt that this coupled with the already small desired signal level on the cable, due to mismatch and the position relative to the main lobe of the antenna, can explain some of the differences between the measured and computed results for angles ($\theta \geq 90^o$). Further experimentation possibilities include designing a feed network to properly match the antenna and using absorber around the remote mixer, if still necessary.

3.4 Computational limitations:

Due to the relatively small thickness of the substrate of the spiral antenna, the volume of the cavity has to be meshed with a good quality tetrahedral mesh. To account for the rapid variation of the field in the cavity, it is essential that a few layers of elements be present to account for the field variation accurately. This requires a large number of tetrahedral elements and proportionately large number of triangular elements in the aperture surface, which results in a large number of non-zero elements in the system matrix. As the frequency increases the electrical depth of the cavity increases, since the wavelength decreases, which in turn requires smaller tetrahedral elements to meet the field sampling requirement. Hence, the computations are limited to 4 and 5GHz for the cases investigated here. With proper meshing and availability of computational facilities such as parallel computing, this antenna configuration can be accurately analyzed at higher frequencies using the present analysis.

4. CONCLUSIONS

An analysis of cavity-backed elliptically-polarized aperture antennas in a finite rectangular ground plane is carried out using a combined FEM/MoM/GTD technique. Slope diffraction coefficients are successfully used to account for the diffracted field of soft polarization, whose incident field at the diffraction point is zero. The radiation patterns for a circular Archimedean spiral microstrip antenna are computed with a finite rectangular ground plane and compared with the experimental data. Within the computational and experimental limitations both computed and measured radiation patterns show very good agreement validating the analysis presented in this report.

ACKNOWLEDGEMENTS

Authors would like to thank Mr. Carl A. Lipp, Mr. Robert Holt and Mr. Hunter Walden for performing the measurements on the spiral antenna.

REFERENCES

[1] C.J.Reddy, M.D.Deshpande, C.R.Cockrell and F.B.Beck, “Analysis of three dimensional cavity backed aperture antennas using a combined FEM/MoM/GTD technique,” *NASA Technical Paper 3548*, 1995.

[2] C.R.Cockrell and F.B.Beck, “Note on use of slope diffraction coefficients for aperture antennas on finite ground planes,” *NASA Technical Memorandum 110192*, August 1995.

[3] J.Jin, *The Finite Element Method in Electromagnetics*, John Wiley & Sons, Inc., New York, 1993.

[4] C.J.Reddy, M.D.Deshpande, C.R.Cockrell and F.B.Beck, “Finite element method for eigenvalue problems in electromagnetics,” *NASA Technical Paper 3485,*December 1994.

[5] S.M.Rao, D.R.Wilton and A.W.Glisson, “Electromagnetic scattering by surfaces of arbitrary shape,” *IEEE Trans. Antennas and Propagation*, Vol.AP-30, pp.409-418, May 1982.

[6] C.A.Balanis, *Advanced Engineering Electromagnetics*, John Wiley & Sons, New York, 1989.

[7] C.R.Cockrell and P.H.Pathak, “Diffraction theory techniques applied to aperture antennas on finite circular and square ground planes,” *IEEE Trans. Antennas and Propagation*, Vol.AP-22, pp.443-448, May 1974.

[8] COSMOS/M User Guide, *Version 1.70*, Structural Research and Analysis Corporation, Santa Monica CA, May 1993.

[9] H.A.Wheeler, “The radiansphere around a small antenna,” *Proceedings of IRE*, pp.1325-1331, August 1959.

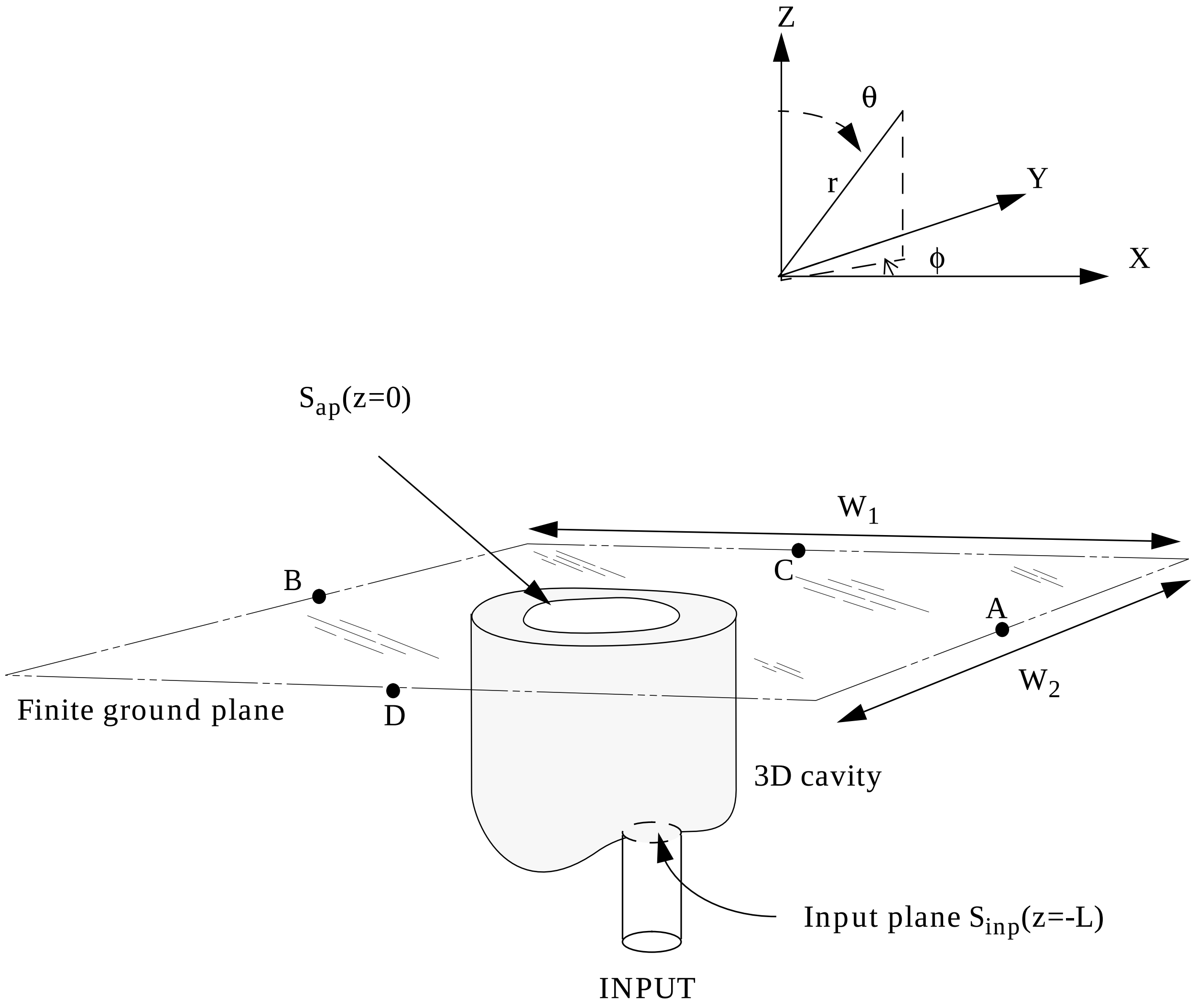

Figure 1 Geometry of a cavity backed aperture in finite ground plane

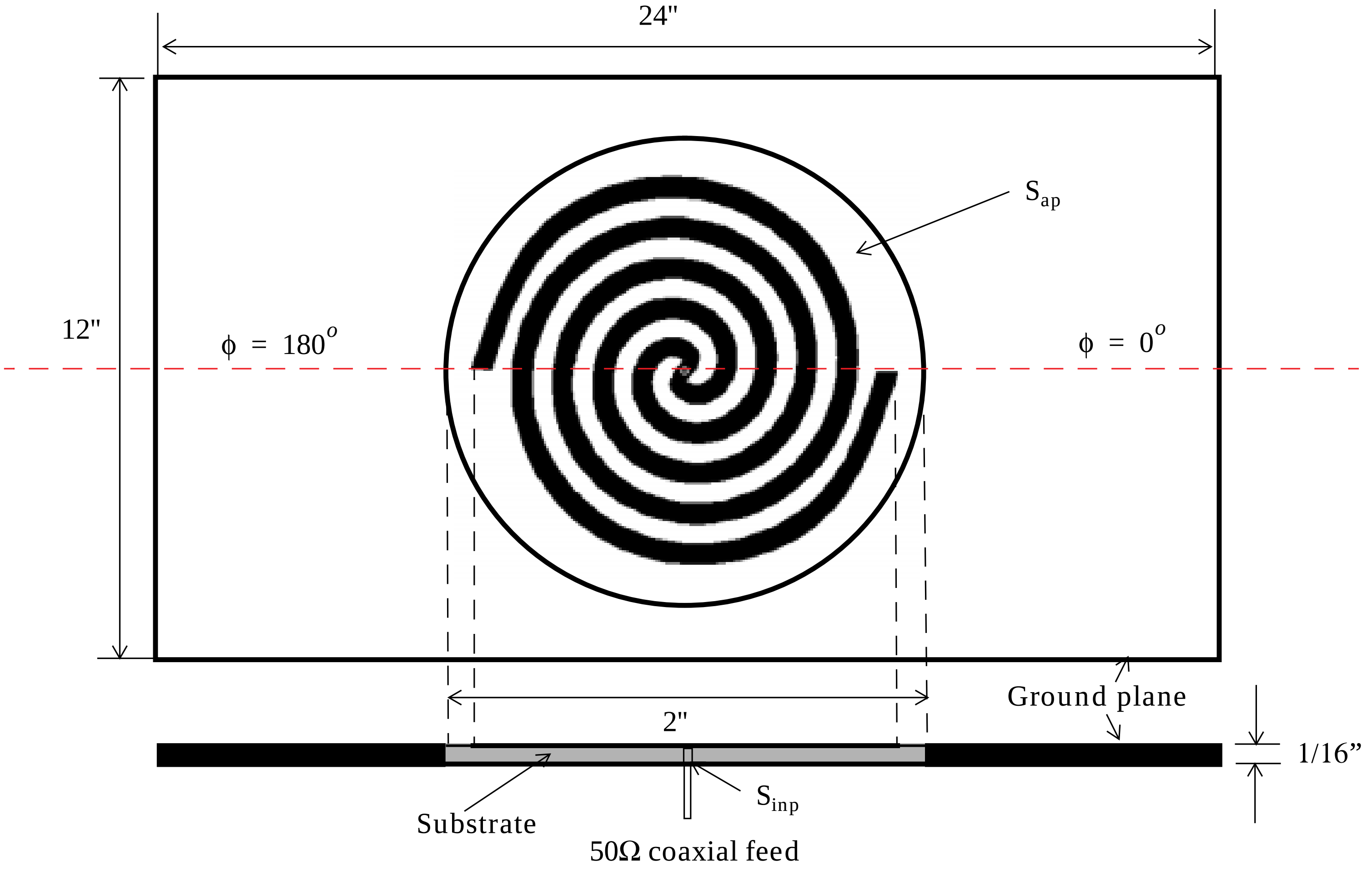

Figure 2 Cavity backed spiral microstrip antenna in a finite ground plane

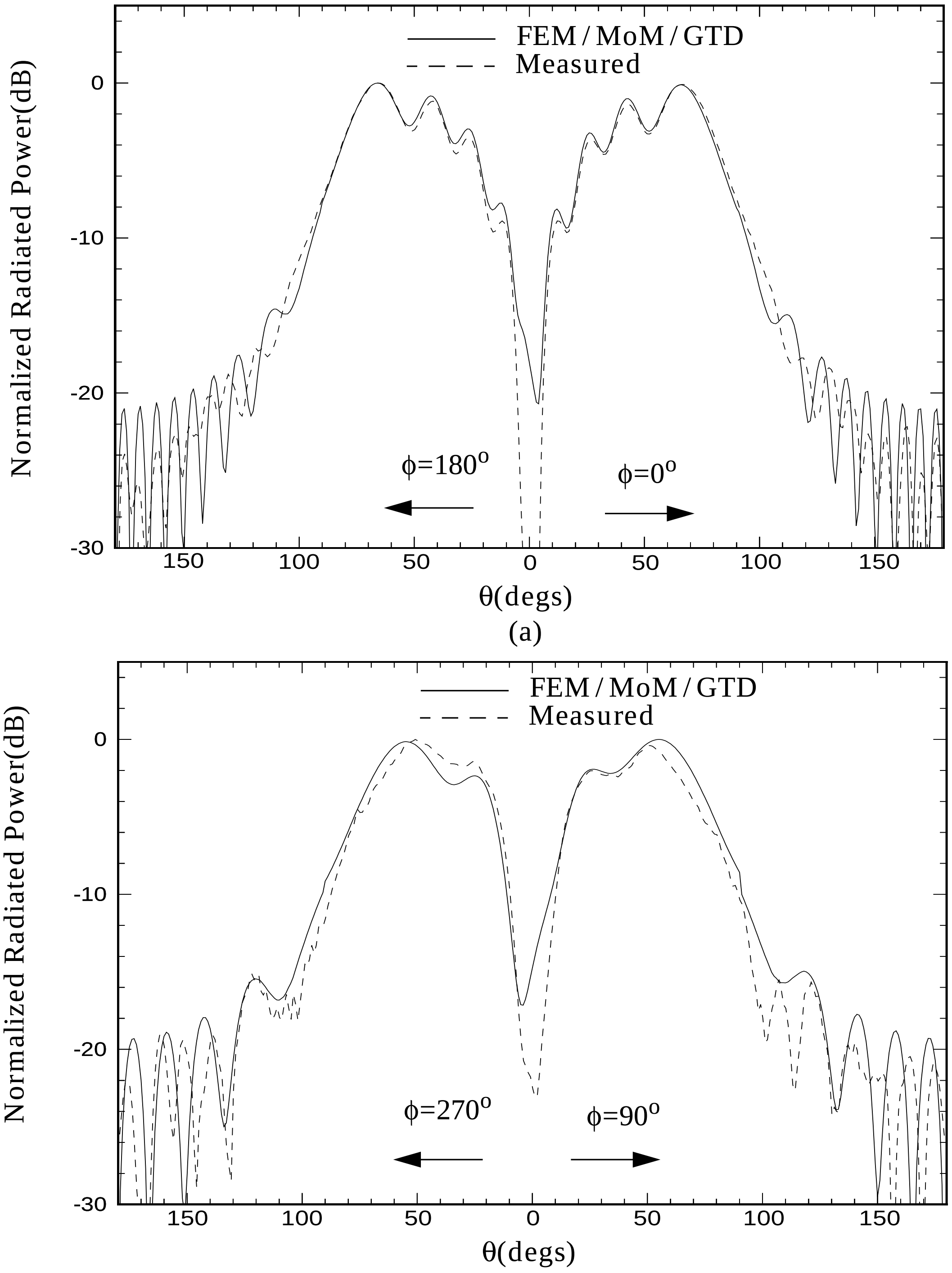

(a)

(b)

Figure 3 Radiation Patterns of spiral antenna (figure 2) at 4GHz-Horizontal(E_θ) Polarization

(a) $\phi=0^o$ and $\phi=180^o$
(b) $\phi=90^o$ and $\phi=270^o$

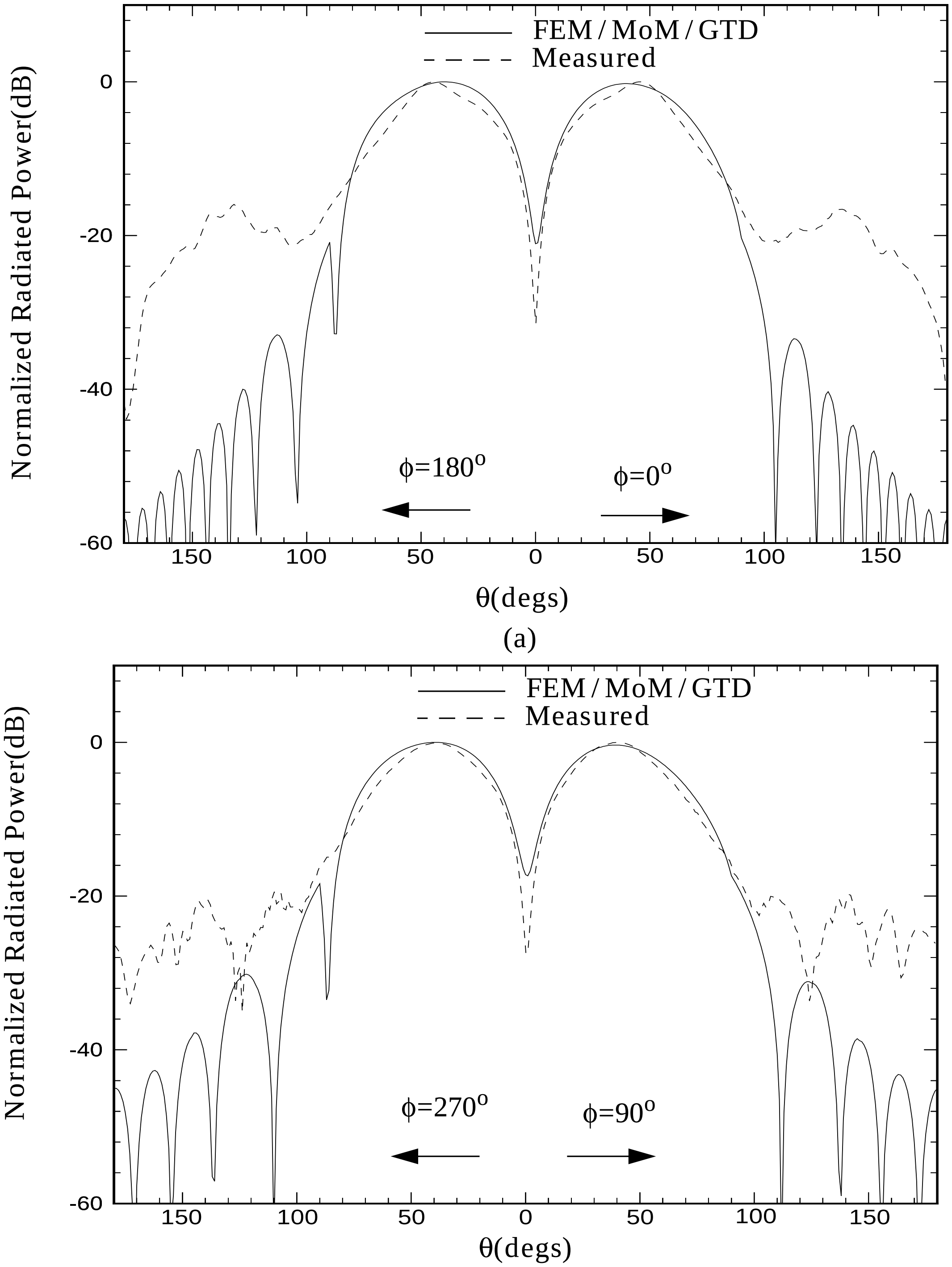

(a)

(b)

Figure 4 Radiation Patterns of spiral antenna(figure 2) at 4GHz - Vertical(E_ϕ) Polarization

(a) $\phi=0^o$ and $\phi=180^o$
(b) $\phi=90^o$ and $\phi=270^o$

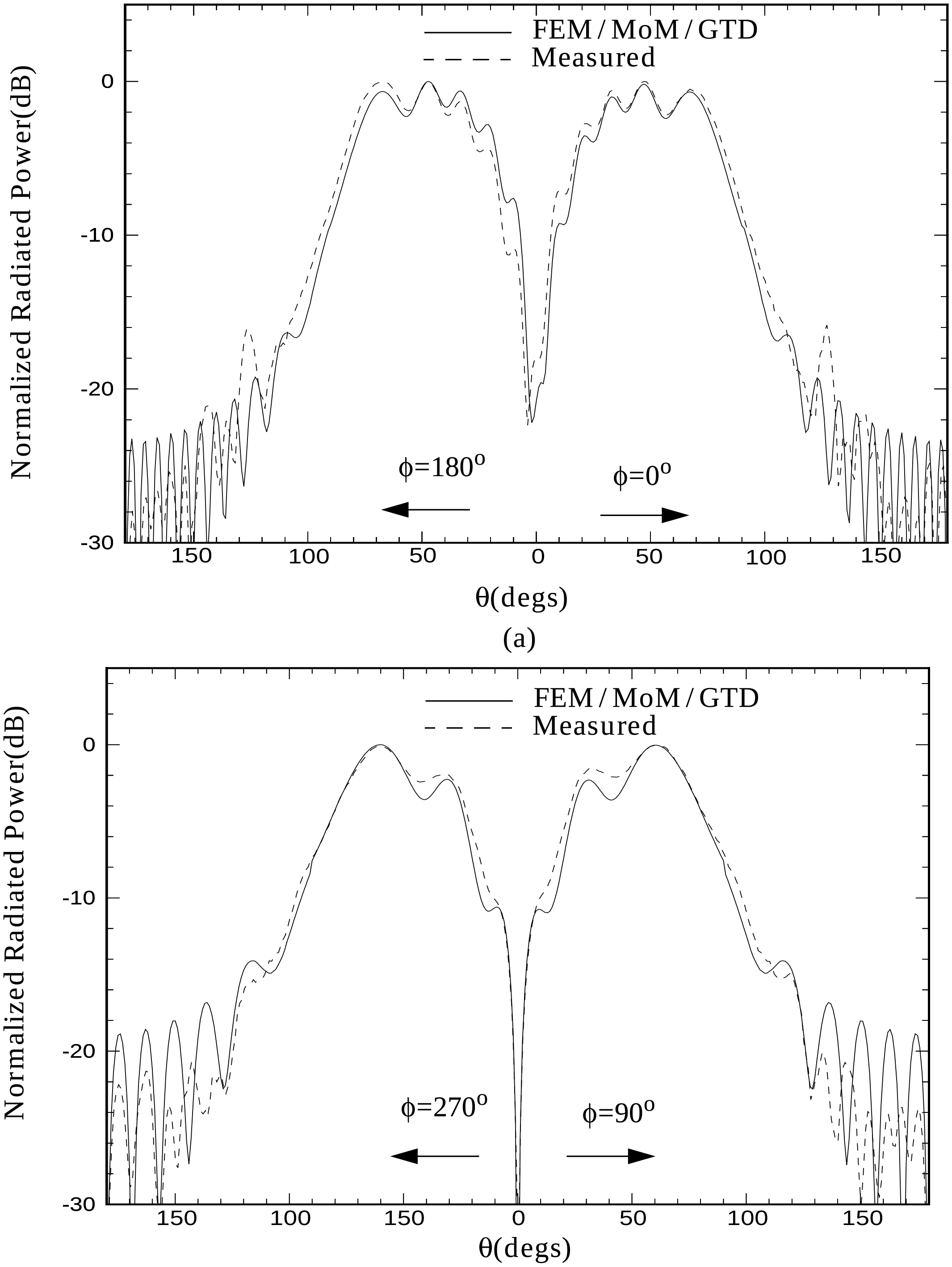

(b)

Figure 5 Radiation Patterns of spiral antenna(figure 2) at 5GHz-Horizontal(E_θ) Polarization

(a) $\phi=0^o$ and $\phi=180^o$
(b) $\phi=90^o$ and $\phi=270^o$

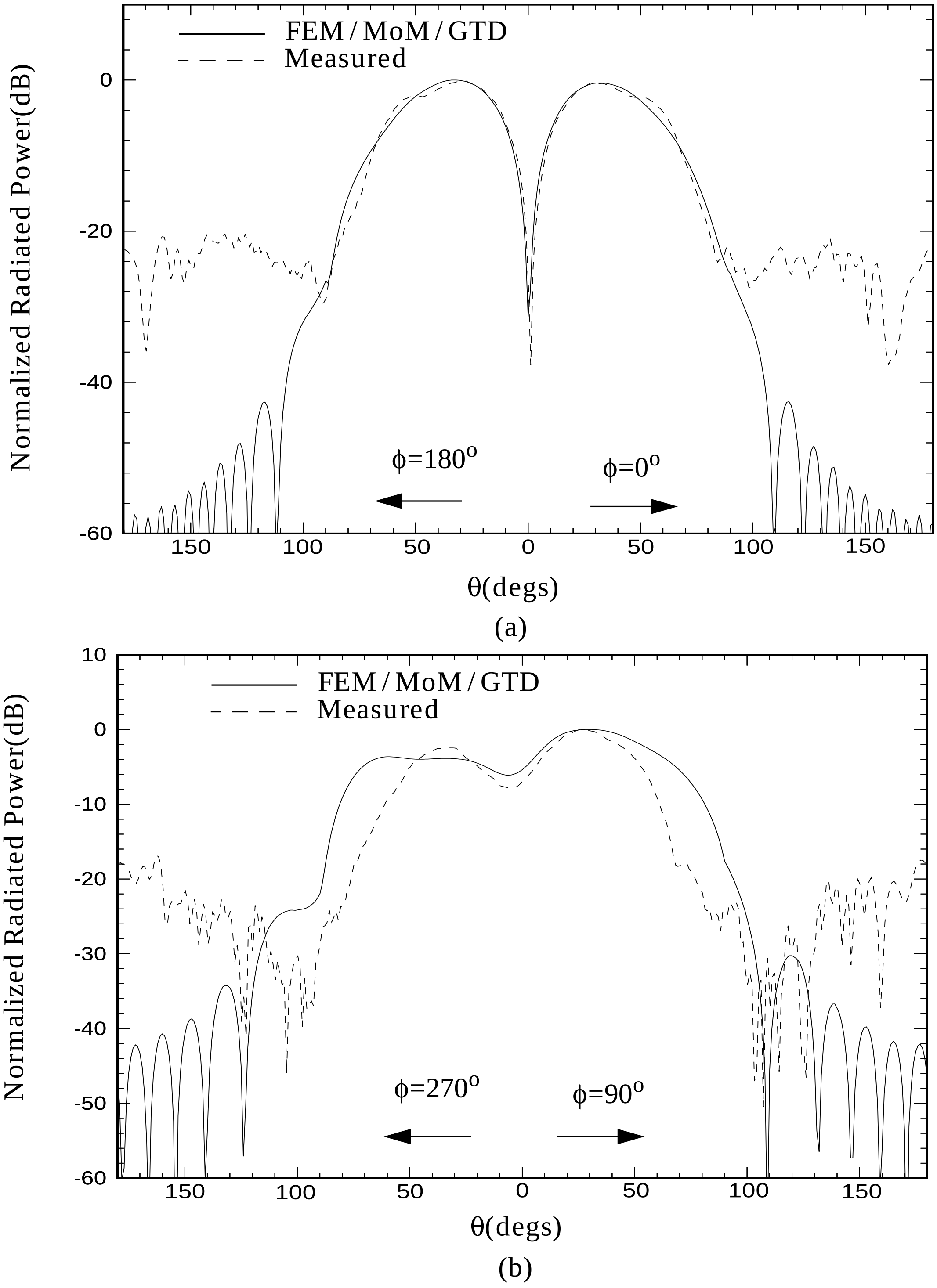

Figure 6 Radiation Patterns of spiral antenna(figure 2) at 5GHz - Vertical(E_ϕ) Polarization

(a) $\phi=0^o$ and $\phi=180^o$
(b) $\phi=90^o$ and $\phi=270^o$